



HAL
open science

Elastic strain mapping of plastically deformed materials by TEM

Arthur Després, Salomé Parent, Muriel Véron, Edgar Rauch, Anne Joulain,
Hadi Bahsoun, Christophe Tromas

► **To cite this version:**

Arthur Després, Salomé Parent, Muriel Véron, Edgar Rauch, Anne Joulain, et al.. Elastic strain mapping of plastically deformed materials by TEM. *Ultramicroscopy*, 2024, 265, pp.114010. 10.1016/j.ultramic.2024.114010 . hal-04718360

HAL Id: hal-04718360

<https://hal.science/hal-04718360v1>

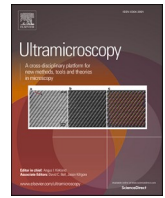
Submitted on 2 Oct 2024

HAL is a multi-disciplinary open access archive for the deposit and dissemination of scientific research documents, whether they are published or not. The documents may come from teaching and research institutions in France or abroad, or from public or private research centers.

L'archive ouverte pluridisciplinaire **HAL**, est destinée au dépôt et à la diffusion de documents scientifiques de niveau recherche, publiés ou non, émanant des établissements d'enseignement et de recherche français ou étrangers, des laboratoires publics ou privés.



Distributed under a Creative Commons Attribution 4.0 International License



Elastic strain mapping of plastically deformed materials by TEM

Arthur Després^{a,*}, Salomé Parent^b, Muriel Véron^a, Edgar F. Rauch^a, Anne Joulain^b, Hadi Bahsoun^b, Christophe Tromas^b

^a Univ. Grenoble Alpes, CNRS, Grenoble INP, SIMaP, F-38000 Grenoble, France

^b Intitut Pprime, Département de Physique et Mécanique des Matériaux, UPR 3346 CNRS - Université de Poitiers – ENSMA, 11 Bd Marie et Pierre Curie, Site du Futuroscope, TSA 41123, Poitiers 86073 CEDEX 9, France

ARTICLE INFO

Keywords:

Transmission electron microscopy
Strains
Dislocations
MAX phases

ABSTRACT

A method for mapping elastic strains by TEM in plastically deformed materials is presented. A characteristic feature of plastically deformed materials, which cannot be handled by standard strain measurement method, is the presence of orientation gradients. To circumvent this issue, we couple orientation and strain maps obtained from scanning precession electron diffraction datasets. More specifically, orientation gradients are taken into account by 1) identifying the diffraction spot positions in a reference pattern, 2) measuring the disorientation between the diffraction patterns in the map and the reference pattern, 3) rotating the coordinate system following the measured disorientation at each position in the map, 4) calculating strains in the rotated coordinate system. At present, only azimuthal rotations of the crystal are handled. The method is illustrated on a Cr₂AlC monocrystal micropillar deformed in near simple flexion during a nanomechanical test. After plastic deformation, the sample contains dislocations arranged in pile-ups and walls. The strain-field around each dislocation is consistent with theory, and a clear difference is observed between the strain fields around pile-ups and walls. It is further remarked that strain maps allow for the orientation of the Burgers vector to be identified. Since the loading undergone by the sample is known, this also allows for the position of the dislocation sources to be estimated. Perspectives for the study of deformed materials are finally discussed.

1. Introduction

Measurement of elastic strain fields by TEM has mostly been applied to semi-conductor materials, where the crystalline structure is almost free from defects [1–4]. In a recent work, however, Rottman and Hemker used scanning precession electron diffraction (SPED) to measure strains around a single dislocation in magnesium [5]. Since then, there have been several attempts to apply this technique to problems involving plastically deformed materials. Some notable examples include the measurements of strain fields around twins in magnesium and steels [6–8], near corrosion-assisted cracks in aluminium alloys [9], and during in-situ tensile testing of stainless steel [10].

With this technique, the acquisition consists in scanning the sample with a nanometric precessed electron beam, and collecting the diffraction patterns at each position [11]. Maps of elastic strains are then obtained from the displacements of the Bragg diffraction spots between the diffraction patterns in the region of interest and a reference pattern taken from a strain-free region of the sample [12,13]. These

displacements must remain small (i.e. not more than a few pixels) for the spot detection algorithm to work efficiently, and for the infinitesimal strain assumption to be valid. For the same reasons, the crystalline orientations in the region of interest must also remain close to that of the reference position.

Plastically deformed materials are known to exhibit orientation gradients, with variations of several degrees over nanometres or micrometres. Orientation gradients are induced by geometrically necessary dislocations and are direct consequence of plastic strain gradients [14,15]. At present, they are not handled by standard strain measurement methods. In the previous examples, this issue was avoided either because the orientation gradient was negligible [9,10] or by selecting a reference pattern for each orientation-wise homogeneous region of the sample [7,8]. Nevertheless, the lack of solutions to handle orientation gradients is a major obstacle to the mapping of elastic strains in plastically deformed materials.

On the other hand, orientation mapping of deformed materials is routine work in the TEM, in particular by automated crystal orientation

* Corresponding author.

E-mail address: arthur.despres@grenoble-inp.fr (A. Després).

<https://doi.org/10.1016/j.ultramic.2024.114010>

Received 23 February 2024; Received in revised form 5 July 2024; Accepted 6 July 2024

Available online 7 July 2024

0304-3991/© 2024 The Author(s). Published by Elsevier B.V. This is an open access article under the CC BY license (<http://creativecommons.org/licenses/by/4.0/>).

mapping (ACOM) [16]. It is notable that the same scanning precession electron diffraction technique is used for orientation and strain mapping. However, there has not been so far attempts to correct strain measurements with the help of orientation maps.

In this paper, we present a method to measure elastic strains in plastically deformed materials which is informed by orientation maps. The method is developed on a particular test case, a Cr_2AlC micropillar deformed by a nanoindentation splitting test, and exhibiting a continuous azimuthal rotation of its crystalline orientations. In the first part of the paper, the method and sample will be presented. A particular focus will be made on the treatment of orientation gradients. In the second part, results coming from two observations will be shown. Finally, perspectives of usage and development for the method will be discussed.

2. Method

2.1. Sample

A monocrystal of Cr_2AlC was used as test case. This material belongs to so-called MAX phases (M for transition metal, A for aluminum or silicon, and X for carbon or nitrogen). It has a hexagonal structure, its space group is $P6_3/mmc$, and its lattice parameters are $a=2.86 \text{ \AA}$ and $c=12.80 \text{ \AA}$ [17]. As for other MAX phases, it has a high c/a ratio (4.47), leading to a plasticity mainly governed, at room temperature, by dislocation slip in the $\langle 11\bar{2}0 \rangle \{0001\}$ system [17–19]. This family of materials is also known to be prone to delamination in the basal plane [20,21].

Single crystal platelets of Cr_2AlC were synthesized by high temperature solution growth at the Laboratoire des Matériaux et du Génie Physique (LMGP) in Grenoble, France, following a protocol established by Ouisse et al. [22]. These platelets have a thickness of about $500 \mu\text{m}$ and a surface of few cm^2 oriented along the basal plane. These platelets were embedded edge-on in a bakelite resina so that the normal to the surface is the $\langle 11\bar{2}0 \rangle$ crystal direction (to be more precise, less than 3.5° from the exact $\langle 11\bar{2}0 \rangle$). The surface was first prepared by conventional mechanical polishing followed by chemo-mechanical polishing. A micropillar with a square section of $3.5 \mu\text{m} \times 3.5 \mu\text{m}$ and a height of around $13 \mu\text{m}$ was milled by focused ion beam (FIB). The sample after milling is shown in the inset of Fig. 1. According to the initial surface orientation, the axis of the pillar is the $\langle 11\bar{2}0 \rangle$ direction (noted \mathbf{a}) and one of the pillar sides is parallel to the basal plane $\{0001\}$ (noted \mathbf{c}).

The pillar was indented with a U-NHT nanoindenter from Anton

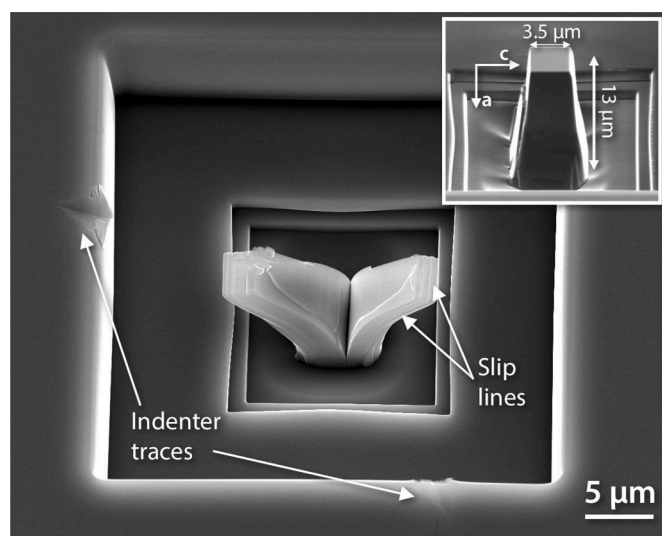


Fig. 1. Scanning electron microscope images of the micropillar after indentation splitting. The initial pillar is shown in the inset.

Paar, using a diamond Berkovich tip in displacement-controlled mode. A vertical fracture appeared abruptly after 200 nm of penetration depth. Since the U-NHT is a “soft machine”, the feedback loop was not fast enough to control the displacement of the indenter, which displaced very fast until it was stopped by the edges of the FIB trench, as shown by the traces in Fig. 1. The acquisition rate of 400 Hz allowed for measurement of the displacement rate, which was of $5 \mu\text{m}$ in 7.5 ms . During the downward motion of the Berkovich indenter, the crack propagated further into the basal plane and the left and right parts of the pillar were pushed on the sides.

The splitting of micropillars during nanoindentation is a well-known outcome for brittle materials [23,24], and also for other MAX phases [25]. However, the remarkable feature in this sample is that, despite the initial fracture, the two parts of the split pillar maintained their integrity and deformed plastically. Slip lines, visible on the initial pillar top surface and on the side surfaces, attest of the basal plane bending. These lines are consistent with dislocations of Burgers vector \mathbf{a} gliding in the basal plane.

2.2. Preliminary observations and acquisition

A thin slice of the sample was cut by focused ion beam (FIB) through the (\mathbf{a}, \mathbf{c}) plane for observation in the transmission electron microscope. Observations were carried out with a FEI-TALOS and a JEOL 2100F both equipped with a field emission gun operating at 200 kV . A bright-field image of the sample is shown in Fig. 2a. The cut is made in the (\mathbf{a}, \mathbf{c}) plane. The diffraction patterns in Fig. 2a and c show the \mathbf{a}^* direction (parallel to the $11\bar{2}0$ spot) and \mathbf{c}^* direction (parallel to the 0002 spot).¹ The crystal rotations are azimuthal (i.e. the rotation axis is normal to the observation plane) and follow the sample curvature. This is consistent with Fig. 1, which showed the bending of the basal planes.

A large bright-field image taken in $1\bar{1}00$ zone axis is shown in Fig. 3. Dislocations are arranged either in pile ups (parallel to the basal planes and spreading from the initial top surface to the sample base) or in walls (perpendicular to the basal plane). This is the expected dislocation structure in plastically deformed MAX phases [20,25]. Among the three possible \mathbf{a} Burgers vector, the $[11\bar{2}0]$ vector, i.e. that which is in the plane of observation, is the one that would experience the highest shear in bending. As a result, all these dislocations are edge or near-edge dislocations with $[11\bar{2}0]$ Burgers vector and $[1\bar{1}00]$ line.

Scanning precession electron diffraction was carried out in the JEOL 2100F microscope, using the DigiSTAR precession device distributed by NanoMegas (Belgium). The convergence angle was 2.2 mrad . A first area of interest was mapped at mid-height in the left part of the sample, near the (b) spot in Fig. 2a. The step size was 2.5 nm . The precession was set to an angle of 1° and with a frequency of 300 Hz . The diffraction patterns were acquired with an in-line direct electron detector Medipix implemented in the Cheetah camera from Amsterdam Scientific. The rate of acquisition was set to 100 frames per second. The patterns were stored in 16bits format with a 512×512 pixel resolution. A second area of interest was mapped near the sample base, at the same location as the (c) spot in Fig. 2a.

Fig. 4a shows a virtual bright-field image of the first area. This image is constructed by numerically integrating the intensity of the transmitted beam for each acquired diffraction pattern, see methodology in ref. [26]. Each dark dot corresponds to a dislocation whose line is normal to the foil. The two dislocations structures can be distinguished. On the first hand, pile-ups are constituted of dislocations in the exact same basal plane and aligned in the \mathbf{a} direction. On the other hand, dislocation walls are formed by dislocations stacking on each other in the \mathbf{c} direction.

Fig. 4b shows the φ_1 Euler angle measured by ACOM on the same map. This angle suffices to fully describe the variations of crystalline

¹ By convention, in this paper, \mathbf{a} and \mathbf{c} refer to directions in the real space, while \mathbf{a}^* and \mathbf{c}^* refer to directions in the reciprocal space.

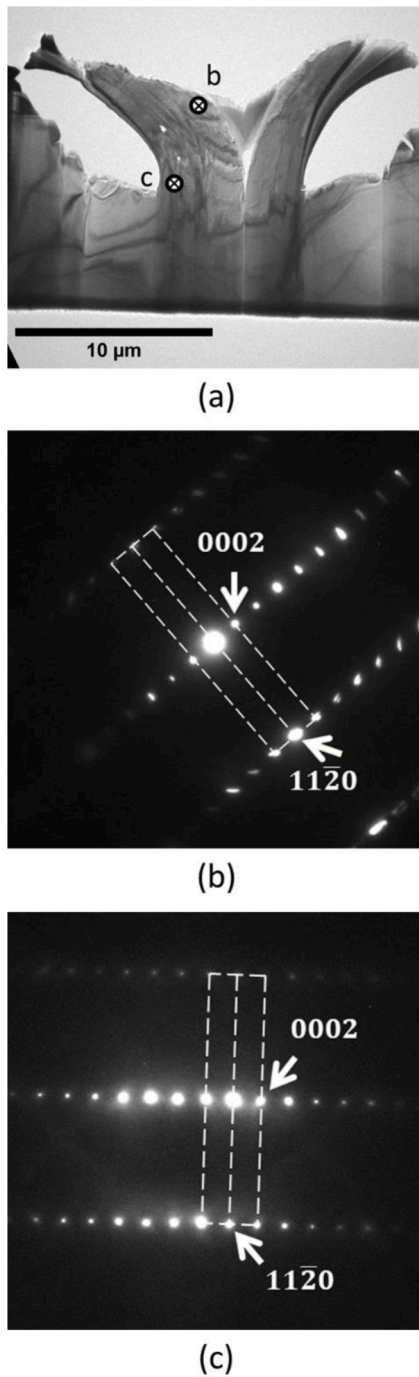


Fig. 2. (a) bright-field image of the FIB sample taken in $\bar{1}\bar{1}00$ zone axis. (b) Selected area diffraction pattern taken in the middle of the sample height. (c) Selected area diffraction pattern taken near the sample base. The real and reciprocal coordinate systems are aligned. The basal plane is normal to the 0002 diffraction vector.

orientations, since the rotations are azimuthal (the two other Euler angles were remarkably constant, with $\Phi = 89.9^\circ \pm 0.1^\circ$ and $\varphi_2 = 60^\circ \pm 0.1^\circ$). Dislocation walls are associated with a sharp change of orientation. For example, in the wall indicated by a double arrow in Fig. 4a, the misorientation angle is 0.78° (average taken over three profiles along the height of the wall). In the same wall, the average dislocation spacing is 21.5 nm. If we assume that the wall is constituted of perfect edge dislocations, with a Burgers vector of 2.86\AA , the predicted misorientation angle is 0.76° . This gives confidence in the accuracy of the measurement. By contrast, dislocation pile-ups do not induce

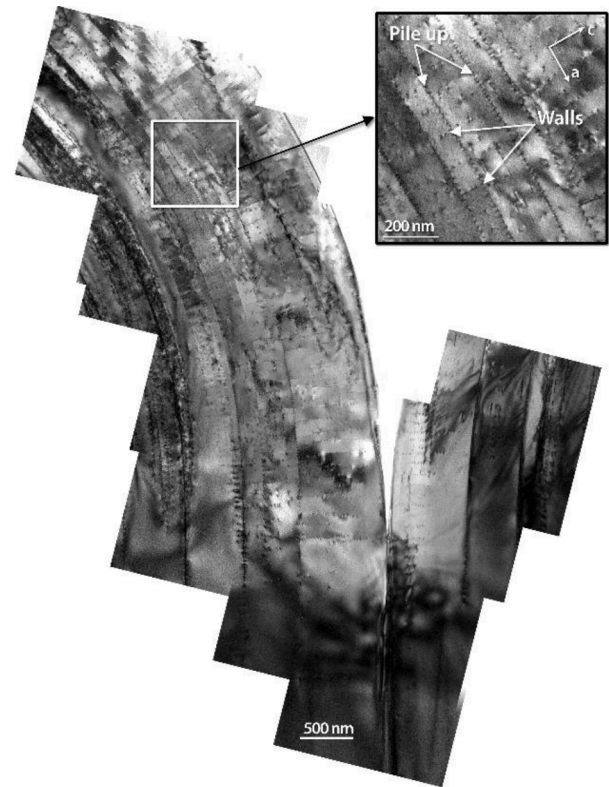


Fig. 3. bright-field image (in $\bar{1}\bar{1}00$ zone axis) showing the dislocation pile ups and walls in the FIB sample.

sharp crystalline rotations, except very locally.

Dislocations in walls are geometrically necessary dislocations since they accommodate orientation gradients. Pile-ups are also geometrically necessary dislocations, but as they do not induce a sharp orientation gradient, it may be difficult to agree with this statement at first sight. However, they fully satisfy the definition given by Ashby [14], namely that regardless of the lengthscale at which their Burgers circuit is drawn, their net Burgers vector is the sum of all dislocations Burgers vector in the pile-up. This point will be further discussed later.

2.3. Strain calculation

The orientation gradients measured in this sample are a typical example of features that cannot be handled by standard strain measurement methods. As a result, a more advanced method was developed. In the first step, the Bragg spots positions are detected with sub-pixel precision on all diffraction patterns. This is achieved using image registration libraries in Python, as previously described in ref. [27]. Fig. 5a and b illustrate the Bragg spot detection on the reference pattern and on another random diffraction pattern. The positions are measured relative to the transmitted beam position, and in the camera coordinate system (x^*, y^*) .

In the second step, the positions are stored as 2 by n matrices, noted G_{ref} and G , with n the number of diffraction spots taken into account. These matrices are then rotated by angles φ_1^{ref} (for the reference pattern) and φ_1 (for all other patterns) in order to calculate the Bragg spots positions in the crystal coordinate system (a^*, c^*) . The corresponding rotation matrices are noted R_{ref} and R , respectively.

In the third step, strains are calculated. The deformation gradient tensor D that transforms the Bragg spot positions measured in the reference pattern into those measured in the other diffraction patterns is then given by:

$$RG = DR_{ref}G_{ref}$$

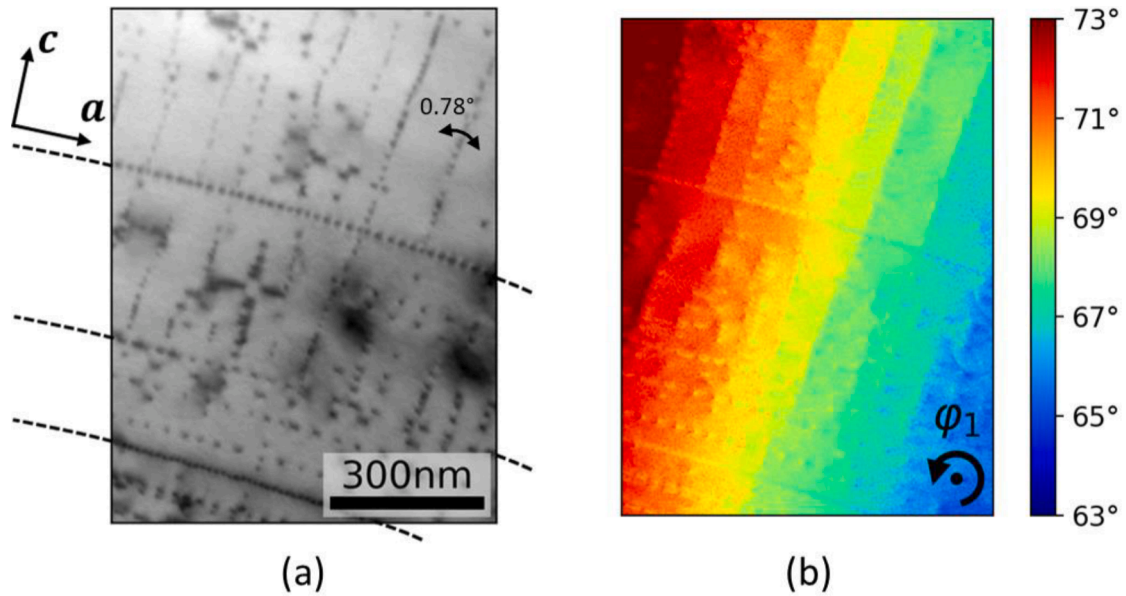


Fig. 4. (a) Virtual bright-field of the scanned area. (b) Map of the φ_1 angle. In (a) the projection of the basal plane is extended out of the map. The indentation direction is close to the vertical axis.

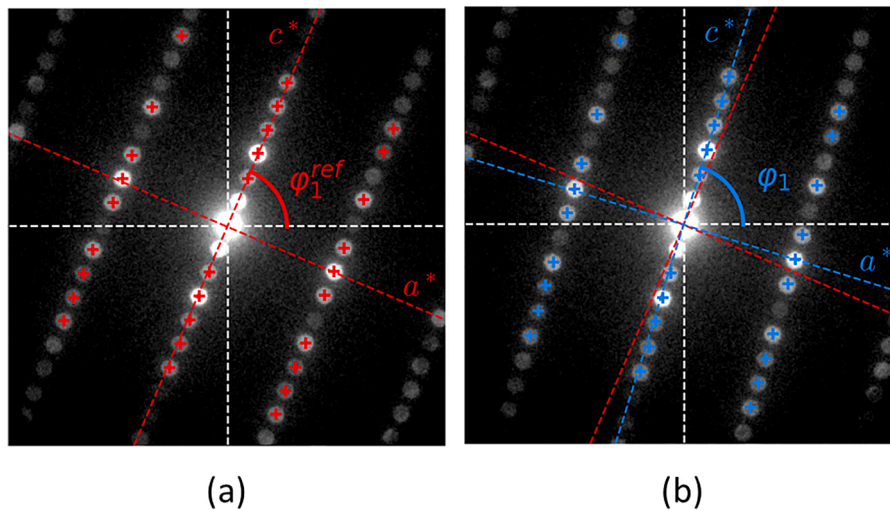


Fig. 5. (a) The reference diffraction pattern. The red dots indicate the centre of the Bragg spots used for strain calculation. The φ_1^{ref} angle corresponds to the rotation between the camera coordinate system (x^* , y^*) and the crystal coordinate system (a^* , c^*). (b) A random diffraction pattern of the dataset, with the centres of the same Bragg spots shown in blue. The orientation of the crystal coordinate system of the reference is left in red, while that of this diffraction pattern is shown in blue. Only the most intense spots have been considered. The first spots on the c^* row have also been discarded because of their proximity with the transmitted beam.

This equation is overdetermined since \mathbf{D} is a 2 by 2 matrix, while \mathbf{G} and \mathbf{G}_{ref} are 2 by n matrices. As a result, \mathbf{D} is solved by linear regression. Finally, in the hypothesis of infinitesimal strains and rotations, \mathbf{D} contains the information about the in-plane strain components, which can be extracted following [8,12,27]²:

$$\begin{bmatrix} \varepsilon_{aa} & \frac{1}{2}(\varepsilon_{ac} - \omega) \\ \frac{1}{2}(\varepsilon_{ac} + \omega) & \varepsilon_{cc} \end{bmatrix} = -(\mathbf{D} - \mathbf{I})$$

² To be consistent with mathematical conventions, transformation and rotation matrices are placed on the left of position matrices. This was not the case in previous publications [8,27].

Where ε_{aa} and ε_{cc} are the longitudinal strains in the a and c directions, ε_{ac} is the in-plane shear strain, \mathbf{I} the identity matrix, and ω is the infinitesimal rotation attributed to the elastic shearing of the crystal. The right term of the equation contains a negative sign to account for the fact that strains in the real space are calculated from positions in the reciprocal space.

With this workflow, strains are calculated in the (a, c) coordinate system. This choice is made because, in the present case, the dislocations Burgers vector follow the rotation of the coordinate system, and therefore, so too do the strain fields induced by dislocations. However, for more usual cases, one may be interested to calculate strains in a classic (x, y) system. This would require to apply different rotations to the matrices of spot position. The workflow to calculate strains in the (x, y) system in the presence of an orientation gradient is described in Appendix A.

It must also be reminded that the reference pattern is supposed to be taken from a strain-free region of the sample. However, in this sample, identifying this region is difficult. For simplicity, the reference pattern has here been selected manually, as much as possible away from dislocations, and so as to result in an approximately even distribution of tensile and compressive strains after calculation. As a result, the values of strains given in the following examples should not be taken as absolute values.

3. Results

Fig. 6 shows the bright-field image and, on the same area, the measured strain fields ϵ_{aa} , ϵ_{ac} , ϵ_{cc} . It is reminded that the area was taken at mid-height in left part of the sample, near the (b) symbol in Fig. 2. It can be first be remarked that the strain fields are indicative of edge dislocations of $+a$ Burgers vector (in the RH/FS convention with a clockwise rotation of the Burgers circuit). This is the most obvious in the ϵ_{aa} map (Fig. 6b), where dislocations exhibit compressive strains ‘above’ (where the extra half plane of the edge dislocation is located), and tensile strains below. Interestingly, a different signature for dislocation pile-ups and walls is observed. Dislocations pile-ups exhibit strong and continuous tensile strains below and compressive strains above. These strains can be qualified as long-range since they extend a few tens of nanometres away from the pile-ups. By contrast, dislocation walls exhibit only short range strains. The tension-compression dipole extends

only over a few nanometres in distance around each individual dislocation in the walls. The intensity of the ϵ_{aa} strains is overall much lower near dislocations in walls than in near dislocations in pile-ups (in fact, strain around dislocation pile-ups are too intense for the selected strain scale, as visible at the bottom of the image).

The difference in ϵ_{aa} strains around dislocation pile-ups and walls is consistent with the classic continuum mechanics theory [28,29]. On the one hand, long-range strain fields of dislocations in pile-ups accumulate, which gives rise to these intense tensile and compressive regions. On the other hand, the long-range strain fields in walls cancel-out, and, as a result, only short-range strain fields remain. While strain fields around individual dislocations have been measured in previous works [5,30], or near grain boundary dislocations [30,31], to our best knowledge these observations provide the first experimental evidence of differences in strain field as a function of the dislocation arrangement.

On the ϵ_{ac} strain map (Fig. 6c), a positive-negative shear dipole is visible around each dislocation. The intensities are overall weaker than for the ϵ_{aa} component because there is no development of long-range ϵ_{ac} strain fields for walls and within pile-ups. Therefore the ϵ_{ac} maps is the closest to showing the contribution of individual dislocations taken separately from each other. On the ϵ_{cc} strain map (Fig. 6d) dislocation pile-ups exhibit long-range tensile strains above them, and compressive strains below them. According to the theory, individual edge dislocations have a short-range ϵ_{cc} strain field with 6 lobes of alternating positive and negative strains. However, when embedded in pile-ups, the

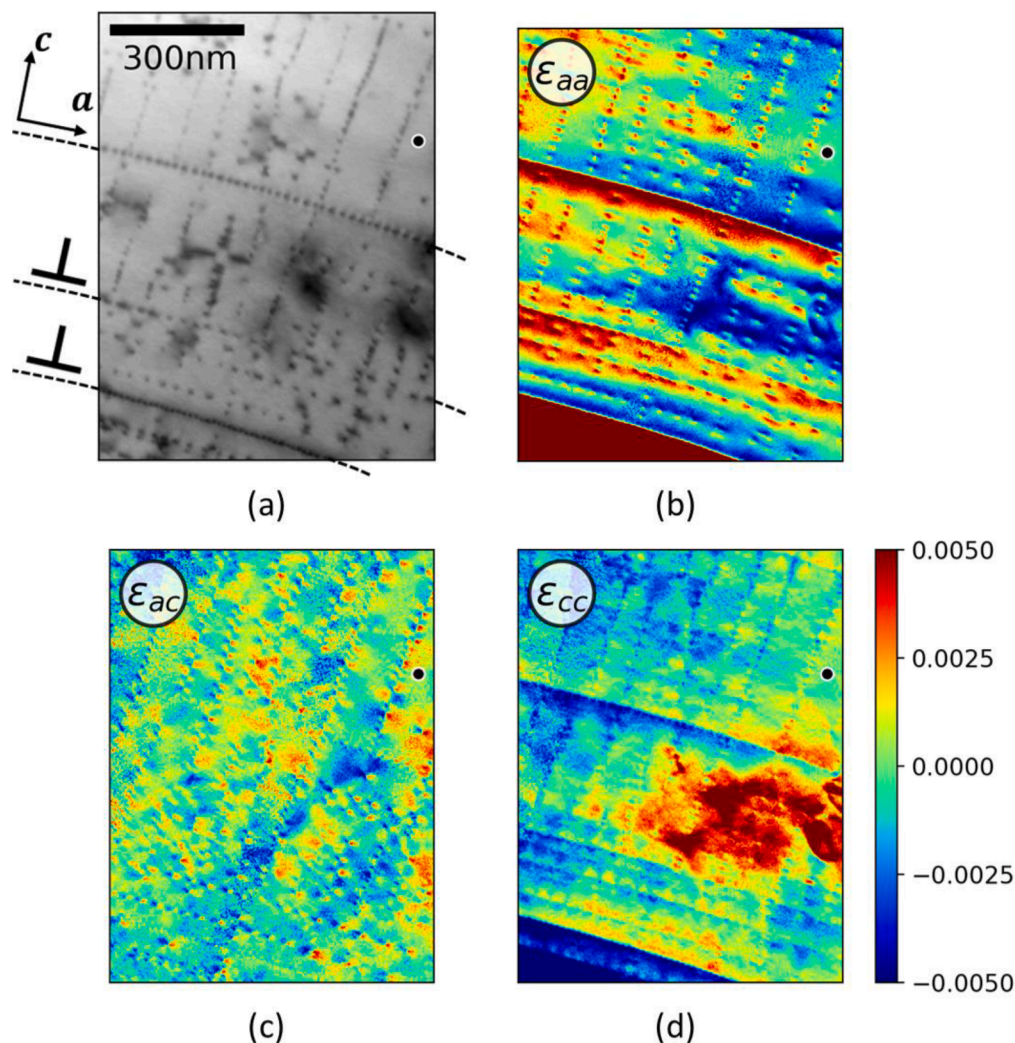


Fig. 6. (a) Virtual bright-field image of the area taken at mid-height of the sample. (b-d) Strain maps measured in the same area. The area corresponds to the ‘b’ mark in Fig. 2. The location of the reference pattern is marked by a black dot. The strain scale is the same for all maps.

long-range strain field is indeed tension above and compression below. It is not a well acknowledged fact in the literature, but it can easily be reproduced using analytical formulas provided in textbooks [28,29].

Again on the ε_{cc} strain map (Fig. 6d), a large region without clear bounds is measured to be in tension. This area coincides approximately with the blurry dark contrast seen the bright-field image (Fig. 6a). It seems to be the signature of ‘mottling’, a defect traditionally observed in other layered materials, such as micas [32,33]. This defect is known to be associated with a ‘mottled’ contrast on bright-field images, and strong variations of the c axis [32]. It is not clear from the literature if this defect already exists in the bulk state or if it results from the interaction between the sample and the electron beam. In any case, it is a real feature of the material, and not an error of measurement (as a matter of fact, the variations of c axis between regions in and out of the mottled region are visible by eye on the diffraction patterns).

Fig. 7 shows similar observations for the second area investigated. It is reminded that it was taken at the sample base, near the (c) symbol in Fig. 2. In this region the crystalline orientations are almost constant, and the (a, c) frame can be considered as the classic (x, y) frame given in textbooks. The field of view is shown at a higher magnification than Fig. 6 to better highlight the strain fields around individual dislocations. Due to the orientation of the crystal in this area, the slip plane is now vertical. The bright-field image shows that only dislocation pile-ups are present (Fig. 7a). As for the previous case, the strain fields are characteristic of edge dislocation with $a + a$ Burgers vector (Fig. 7b-d). Interestingly, the dislocation spacing in the pile-ups tends to increase towards the base of the sample (i.e. towards the bottom of the image). This evolution coincides with a decrease of the long-range strain-fields ε_{aa} and ε_{cc} from the top to the bottom of the image. Consequently, the short-range strain fields around individual dislocations are more easily distinguished at the bottom of the image.

In Fig. 7, around the most isolated dislocations (mostly in the bottom of the image), it can be noticed that the intensity of the strain ε_{ac} and ε_{cc} components is quite close to the background level. This is because the intensity of strains around individual dislocations is not that high for those components at this resolution. If one seeks to image strain fields at a higher resolution nearer the dislocation core, it is likely that other

techniques should be preferred, such as the geometric phase analysis (GPA) using high-resolution TEM.

4. Discussion

4.1. Position of the dislocations sources

One consequence of knowing the Burgers vector orientation is that, if the mechanical path of the sample is known, the position of the dislocation sources can be retrieved. As described above, the sample was first fractured in two parts, which were then pushed in opposite directions by the indenter tip. The loading applied to each part of the sample can be considered as approaching a simple flexion test, with longitudinal stresses σ_{aa} and shear stresses τ_{ac} developing in reaction to imposed horizontal displacements. Because of the particular orientation of the crystal relative to the loading direction, the longitudinal stresses σ_{aa} induce no resolved shear stress on the $\langle 11\bar{2}0 \rangle \{0001\}$ slip system. Therefore, dislocations slip operates only due to the shear stresses τ_{ac} . These stresses have a parabolic profile along the c axis, are null at the free surfaces and maximal at the central fiber according to the Timoshenko elasticity theory [34].

In the left part of the sample, all dislocations are edge or near edge dislocations with $a + a$ Burgers vector. As a result, to accommodate the shear stresses τ_{ac} and induce the steps visible on the upper surface (Fig. 1), these dislocations must come from the upper surface and slip towards the sample base. Dislocation sources operating at free surfaces generate half Frank-Read loops [29,35,36], with dislocation segments having, in this configuration, only $+a$ Burgers vectors. As the dislocation slips towards the sample base, the radius of the loop increases, and the dislocation segments progressively acquire a more edge character. The process is illustrated in Fig. 8. In the unlikely event that a few dislocation sources had operated within the sample, full dislocation loops with segments having $-a$ and $+a$ Burgers vector would have been generated, with the $-a$ segments slipping towards the sample upper surface. However, due to the excess of $+a$ dislocation coming from the upper surface, the $-a$ dislocations would have been quickly annihilated. We find this scenario fully consistent with the observations.

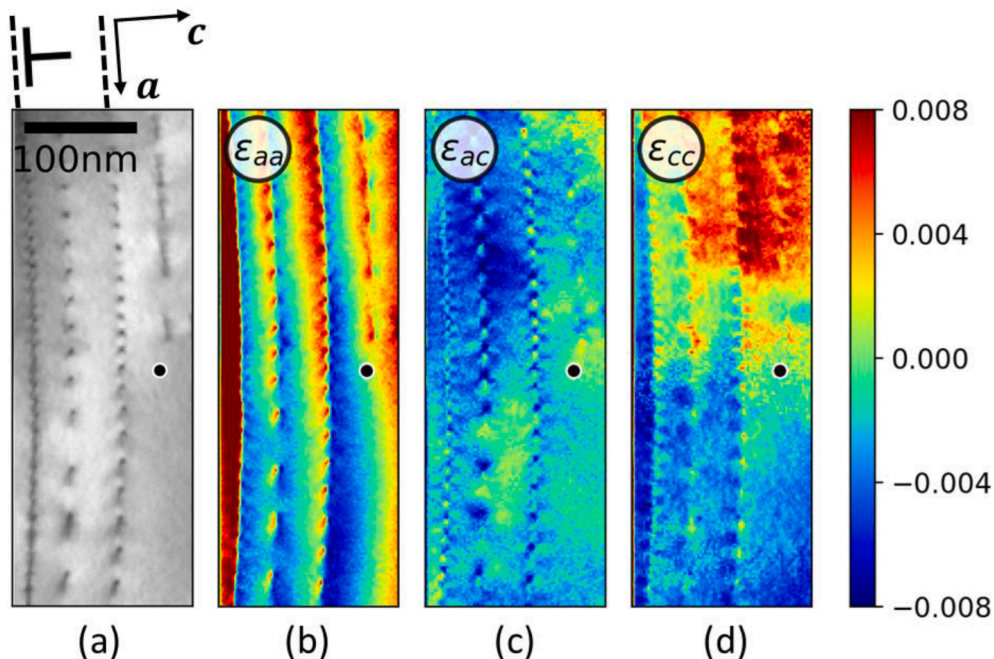


Fig. 7. (a) Virtual bright-field image of the area taken near the sample base. (b-d) Strain maps measured in the same area. The area corresponds to the ‘c’ mark in Fig. 2. The location of the reference pattern is marked by a black dot. The strain scale is the same for all maps.

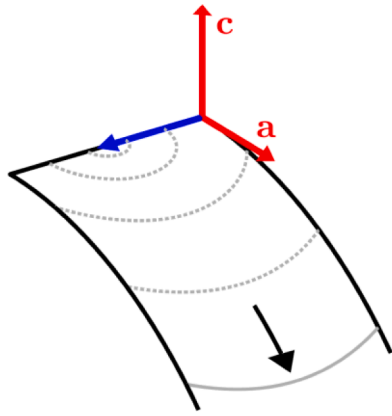


Fig. 8. Schematic 3D view of the slip of a dislocation on a bent basal plane. The dislocation nucleates from a half Frank-Read loop at the top surface, and slips towards the sample base, as indicated by the black arrow. Dislocation segments parallel to the blue axis have an edge character, while segments parallel to the a axis have a screw character. As a reminder, the (a, c) plane is the observation plane in the TEM.

4.2. On geometrically necessary dislocations

It has been pointed out above that considering the dislocations in pile-ups as geometrically necessary dislocations is not obvious. This likely comes from the idea that we are often tempted to believe that geometrically necessary dislocations should induce crystalline rotations, while dislocations in pile-ups do not. However, dislocations in pile-ups are indeed geometrically necessary because they satisfy the theoretical definitions [37,38]. For a given Burgers circuit drawn around a group of dislocations, the geometrically necessary dislocations are those that induce the net Burgers vector measured in this circuit. In mathematical terms, the net Burgers vector B can be decomposed into nb with n the number of geometrically necessary dislocations, and b their Burgers vector. If a Burgers circuit is drawn around dislocations in a pile-up, as all dislocations have the same Burgers vector (with the same sign), the net Burgers vector is exactly the number of dislocations within the pile-up times the Burgers vector of a single dislocation. Therefore, dislocations in pile-ups are indeed geometrically necessary dislocations, regardless of the lengthscale of the Burgers circuit.

A complementary description of geometrically necessary dislocations is the Nye tensor. Geometrically necessary dislocations are those that induce a non-null Nye tensor. For edge dislocations in the configuration studied here, the only non-null Nye tensor component is α_{13} , and the density of geometrically necessary dislocations measured per pixel is $\rho = \alpha_{13}/b = \left(\frac{\partial \varepsilon_{aa}}{\partial c} - \frac{\partial \varepsilon_{ac}}{\partial a} + \frac{\partial \psi_1}{\partial a} \right) / b$ [39,40]. The first two terms in parenthesis describe the elastic curvature, and the third term³ is the gradient of orientation (i.e. the crystalline rotation). By comparing the orientation and strain maps, it becomes possible to realize that term ‘geometrically necessary dislocation’ may include in fact very different types of dislocation structures: dislocations in pile-ups are geometrically necessary mostly because they induce elastic strain gradient (in particular gradients in ε_{aa}), while dislocations in walls are geometrically necessary because they induce orientation gradients.

4.3. Perspectives of application to deformed materials

Dislocation pile-ups and walls are two fundamental features of

³ Note that the sign in front of $\frac{\partial \psi_1}{\partial a}$ may change as a function of the chosen coordinate system and sense of rotation (see on this topic ref. [40]). This formula is shown here only for discussion purposes.

plastically deformed materials, with different effects on strain hardening. Dislocations in walls contribute to isotropic hardening by a rather simple forest dislocation mechanism, while pile-ups mostly affect strain hardening in a kinematic way, by inducing back-stresses when meeting grain boundaries and free surfaces [28,29]. Models describing hardening during plastic deformation are far from having acquired a stable form. For example, some consider that back-stresses have a transient effect on hardening [41] while other consider that a permanent effect remain even after large deformation [42]. With the method presented here, one could potentially investigate the phenomena contributing to isotropic and kinematic hardening, at the microstructure level, and at different stages of deformation.

As mentioned in the introduction, orientation gradients are prevalent in plastically deformed materials. It is mostly their presence which limits the use of standard TEM strain measurement methods (the elastic curvature is less problematic in that regard). The method proposed in this work can be seen as a first step to correct the effect orientation gradients on strain mapping in the TEM. In this example case, only azimuthal rotations were taken into account. However, in a randomly oriented crystal and in polycrystals, rotations can be in any direction. Zenithal (i.e. out-of-plane) rotations would modify the number and position of spots appearing on the diffraction patterns. It would certainly be more challenging because, at present, strain measurement methods rely on detecting features which should be present in all diffraction patterns. In order to map elastic strains in any plastically deformed material, future implementations should therefore focus on handling this kind of rotation.

5. Conclusion

A method was developed to map elastic strains by TEM in materials exhibiting orientation gradients. It uses scanning precession electron diffraction data, and couples crystallographic orientation mapping with calculation of strains from measurements of displacements of the diffraction spots. Knowledge of the orientation allows for the reference coordinate systems to be rotated for each position on the map. This procedure is required to calculate strains according to the infinitesimal strain assumption. For now, only azimuthal rotations are accounted for, but future developments should include out-of-plane rotations in order for the elastic strain fields to be mapped in any randomly oriented crystal.

The method is particularly adapted to plastically deformed materials, which are well known for exhibiting orientation gradients. In the Cr_2AlC sample presented here, the strain maps revealed differences in strain fields induced by dislocation pile-ups and walls. It was also remarked that strain maps allow for the orientation of the Burgers vector to be inferred. If the mechanical path of the sample is known, it then becomes possible to retrieve the position of the dislocation sources. The capability to measure strain fields induced by dislocation structures opens interesting perspectives for the study of strain hardening in plastically deformed materials.

CRediT authorship contribution statement

Arthur Després: Conceptualization, Investigation, Data curation, Writing – original draft. **Salomé Parent:** Investigation, Data curation. **Muriel Véron:** Investigation, Data curation. **Edgar F. Rauch:** Conceptualization, Investigation, Writing – review & editing. **Anne Joulain:** Writing – review & editing, Investigation. **Hadi Bahsoun:** Investigation. **Christophe Tromas:** Writing – review & editing, Investigation, Conceptualization.

Declaration of competing interest

The authors declare that they have no known competing financial interests or personal relationships that could have appeared to influence

the work reported in this paper.

Data availability

Data will be made available on request.

Acknowledgements

This work has benefited from the equipment of the Grenoble INP

CMTC platform supported by the Centre of Excellence of Multifunctional Architected Materials "CEMAM" n°ANR-10-LABX-4401.

Institut Pprime gratefully acknowledges "Contrat de Plan Etat - Région Nouvelle-Aquitaine" (CPER) as well as the "Fonds Européen de Développement Régional" (FEDER) [reference n°2018-3868210 (BACASMET)] for their financial support to the reported work. This work pertains to the French Government programs "Investissements d'Avenir" LABEX INTERACTIFS [reference ANR-11-LABX-0017-01] and EUR INTREE [reference ANR-18-EURE-0010].

Appendix A. Strain calculation in the (x,y) coordinate system

To calculate strains in the (x,y) system, and to satisfy the infinitesimal strain hypothesis, the following formula is applied:

$$G = \tilde{R} \tilde{R} G_{ref}$$

Where \tilde{R} accounts for the rotation of the reference pattern by an angle $\Delta\varphi_1 = \varphi_1^{ref} - \varphi_1$, and G and G_{ref} are still expressed in the (x,y) system. The operation $\tilde{R} G_{ref}$ is equivalent to creating a 'ghost' reference pattern having the same crystallographic orientation as the diffraction pattern of interest. The strain components are then extracted following:

$$\begin{bmatrix} \varepsilon_{xx} & \frac{1}{2}(\varepsilon_{xy} - \delta\omega) \\ \frac{1}{2}(\varepsilon_{xy} + \delta\omega) & \varepsilon_{yy} \end{bmatrix} = -(\mathbf{D} - \mathbf{I})$$

In Fig. A.1a and b, the ε_{aa} map and the ε_{xx} map calculated with the rotation matrix \tilde{R} are compared. Because of the particular orientation of the sample, these two maps are quite similar. Without applying the rotation, the strain map becomes flawed, as shown in Figure A. 1c.

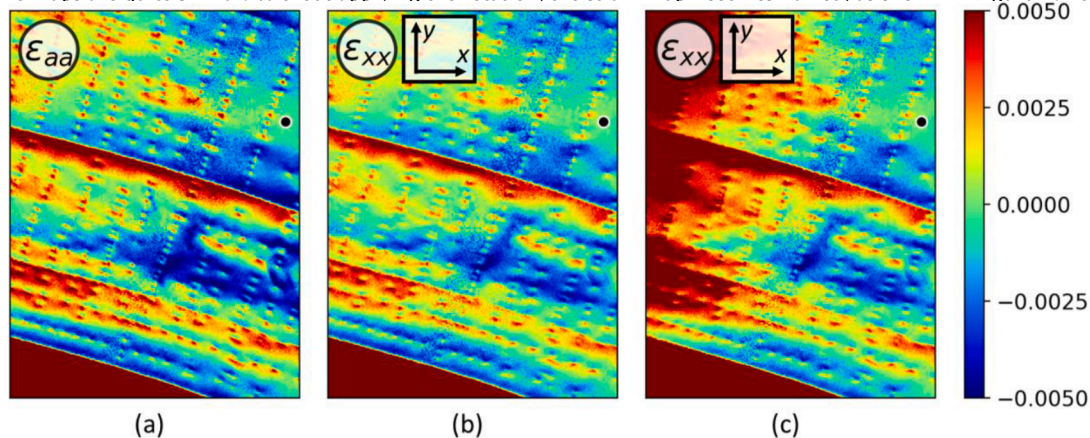


Fig. A.1. (a) ε_{aa} map. (b) ε_{xx} map calculated with the rotation of the reference pattern, i.e. using $G = \tilde{R} \tilde{R} G_{ref}$. (c) ε_{xx} map calculated without rotation of the reference pattern, i.e. using $G = \mathbf{D} G_{ref}$.

References

- [1] A.D. Darbal, R.D. Narayan, C. Vartuli, G. Lian, R. Graham, F. Shaapur, S. Nicolopoulos, J.K. Weiss, Automated High Precision Strain Measurement Using Nanobeam Diffraction Coupled with Precession, *Microsc. Microanal.* 19 (2013) 702–703, <https://doi.org/10.1017/S1431927613005503>.
- [2] J.-L. Rouviere, A. Béché, Y. Martin, T. Denneulin, D. Cooper, Improved strain precision with high spatial resolution using nanobeam precession electron diffraction, *Appl. Phys. Lett.* 103 (2013) 241913, <https://doi.org/10.1063/1.4829154>.
- [3] M.-J. Hÿtch, J.-L. Putaux, J.-M. Pénisson, Measurement of the displacement field of dislocations to 0.03 Å by electron microscopy, *Nature* 423 (2003) 270–273, <https://doi.org/10.1038/nature01638>.
- [4] M. Hÿtch, F. Houdellier, F. Hüe, E. Snoeck, Nanoscale holographic interferometry for strain measurements in electronic devices, *Nature* 453 (2008) 1086–1089, <https://doi.org/10.1038/nature07049>.
- [5] P.F. Rottmann, K.J. Hemker, Nanoscale elastic strain mapping of polycrystalline materials, *Mater. Res. Lett.* 6 (2018) 249–254, <https://doi.org/10.1080/21663831.2018.1436609>.
- [6] B. Leu, M.A. Kumar, P.F. Rottmann, K.J. Hemker, I.J. Beyerlein, Micromechanical fields associated with irregular deformation twins in magnesium, *J. Mater. Eng. Perform.* (2022), <https://doi.org/10.1007/s11665-022-07196-3>.
- [7] T.W.J. Kwok, T.P. McAuliffe, A.K. Ackerman, B.H. Savitzky, M. Danaie, C. Ophus, D. Dye, The mechanism of twin thickening and the elastic strain state of TWIP steel nanotwins, *Mater. Sci. Eng. A.* 873 (2023) 145005, <https://doi.org/10.1016/j.msea.2023.145005>.
- [8] T.C. Pekin, C. Gammer, J. Ciston, A.M. Minor, C. Ophus, Optimizing disk registration algorithms for nanobeam electron diffraction strain mapping, *Ultramicroscopy* 176 (2017) 170–176, <https://doi.org/10.1016/j.ultramic.2016.12.021>.
- [9] M. López Freixes, X. Zhou, R. Aymerich-Armengol, M. Vega-Paredes, L. Peguet, T. Warner, B. Gault, Crack arrest markings in stress corrosion cracking of 7xxx aluminium alloys: insights into active hydrogen embrittlement mechanisms, *Scr. Mater.* 237 (2023) 115690, <https://doi.org/10.1016/j.scriptamat.2023.115690>.
- [10] T.C. Pekin, C. Gammer, J. Ciston, C. Ophus, A.M. Minor, In situ nanobeam electron diffraction strain mapping of planar slip in stainless steel, *Scr. Mater.* 146 (2018) 87–90, <https://doi.org/10.1016/j.scriptamat.2017.11.005>.
- [11] P.A. Midgley, A.S. Eggeman, Precession electron diffraction – a topical review, *IUCr J* 2 (2015) 126–136, <https://doi.org/10.1107/S2052252514022283>.
- [12] A. Béché, J.L. Rouvière, J.P. Barnes, D. Cooper, Strain measurement at the nanoscale: comparison between convergent beam electron diffraction, nano-beam electron diffraction, high resolution imaging and dark field electron holography, *Ultramicroscopy* 131 (2013) 10–23, <https://doi.org/10.1016/j.ultramic.2013.03.014>.

- [13] D. Cooper, T. Denneulin, N. Bernier, A. Béché, J.-L. Rouvière, Strain mapping of semiconductor specimens with nm-scale resolution in a transmission electron microscope, *Micron* 80 (2016) 145–165, <https://doi.org/10.1016/j.micron.2015.09.001>.
- [14] M.F. Ashby, The deformation of plastically non-homogeneous materials, *Philos. Mag.* 21 (1970) 399–424, <https://doi.org/10.1080/14786437008238426>.
- [15] N.A. Fleck, G.M. Muller, M.F. Ashby, J.W. Hutchinson, Strain gradient plasticity: theory and experiment, *Acta Metall. Mater.* 42 (1994) 475–487, [https://doi.org/10.1016/0956-7151\(94\)90502-9](https://doi.org/10.1016/0956-7151(94)90502-9).
- [16] E.F. Rauch, M. Véron, Automated crystal orientation and phase mapping in TEM, *Mater. Charact.* 98 (2014) 1–9, <https://doi.org/10.1016/j.matchar.2014.08.010>.
- [17] M.W. Barsoum, The MN+1AXn phases: a new class of solids: thermodynamically stable nanolaminates, *Prog. Solid State Chem.* 28 (2000) 201–281, [https://doi.org/10.1016/S0079-6786\(00\)00006-6](https://doi.org/10.1016/S0079-6786(00)00006-6).
- [18] J.T. Pürstl, T.E.J. Edwards, F.D. León-Cázares, R.P. Thompson, N.M. Della Ventura, N.A. Jones, W.J. Clegg, The effect of orientation on the deformation behavior of Cr₂AlC, *Acta Mater.* 257 (2023) 119136, <https://doi.org/10.1016/j.actamat.2023.119136>.
- [19] A. Guitton, A. Joulain, L. Thilly, C. Tromas, Dislocation analysis of Ti₂AlN deformed at room temperature under confining pressure, *Philos. Mag.* 92 (2012) 4536–4546, <https://doi.org/10.1080/14786435.2012.715250>.
- [20] M.W. Barsoum, L. Farber, T. El-Raghy, Dislocations, kink bands, and room-temperature plasticity of Ti₃SiC₂, *Metall. Mater. Trans. A.* 30 (1999) 1727–1738, <https://doi.org/10.1007/s11661-999-0172-z>.
- [21] W. Tian, Z. Sun, H. Hashimoto, Y. Du, Compressive deformation behavior of ternary compound Cr₂AlC, *J. Mater. Sci.* 44 (2009) 102–107, <https://doi.org/10.1007/s10853-008-3113-0>.
- [22] T. Ouisse, E. Sarigiannidou, O. Chaix-Pluchery, H. Roussel, B. Doisneau, D. Chaussende, High temperature solution growth and characterization of Cr₂AlC single crystals, *J. Cryst. Growth.* 384 (2013) 88–95, <https://doi.org/10.1016/j.jcrysgro.2013.09.021>.
- [23] P.R. Howie, S. Korte, W.J. Clegg, Fracture modes in micropillar compression of brittle crystals, *J. Mater. Res.* 27 (2012) 141–151, <https://doi.org/10.1557/jmr.2011.256>.
- [24] M. Sebastiani, K.E. Johanns, E.G. Herbert, F. Carassiti, G.M. Pharr, A novel pillar indentation splitting test for measuring fracture toughness of thin ceramic coatings, *Philos. Mag.* 95 (2015) 1928–1944, <https://doi.org/10.1080/14786435.2014.913110>.
- [25] M. Higashi, S. Momono, K. Kishida, N.L. Okamoto, H. Inui, Anisotropic plastic deformation of single crystals of the MAX phase compound Ti₃SiC₂ investigated by micropillar compression, *Acta Mater.* 161 (2018) 161–170, <https://doi.org/10.1016/j.actamat.2018.09.024>.
- [26] E.F. Rauch, M. Véron, Virtual dark-field images reconstructed from electron diffraction patterns, *Eur. Phys. J. Appl. Phys.* 66 (2014) 10701, <https://doi.org/10.1051/epjap/2014130556>.
- [27] A. Després, M. Veron, Elastic strain field measurements in the TEM for metallurgical applications, *Mater. Charact.* 202 (2023) 113012, <https://doi.org/10.1016/j.matchar.2023.113012>.
- [28] D. Hull, D.J. Bacon, *Introduction to dislocations*. Butterworth Heinemann, 5. ed, Elsevier, Amsterdam Heidelberg, 2011.
- [29] P.M. Anderson, J.P. Hirth, J. Lothe, *Theory of Dislocations*, Cambridge University Press, 2017.
- [30] M.J. Hÿtch, J.-L. Putaux, J. Thibault, Stress and strain around grain-boundary dislocations measured by high-resolution electron microscopy, *Philos. Mag.* 86 (2006) 4641–4656, <https://doi.org/10.1080/14786430600743876>.
- [31] M. Couillard, G. Radtke, G.A. Botton, Strain fields around dislocation arrays in a $\Sigma 9$ silicon bicrystal measured by scanning transmission electron microscopy, *Philos. Mag.* 93 (2013) 1250–1267, <https://doi.org/10.1080/14786435.2013.778428>.
- [32] D.C. Noe, D.R. Veblen, Mottled contrast in TEM images of mica crystals, *Am. Mineral.* 84 (1999) 1932–1938, <https://doi.org/10.2138/am-1999-11-1221>.
- [33] C. Ferraris, D. Castelli, B. Lombardo, SEM/TEM-AEM characterization of micro- and nano-scale zonation in phengite from a UHP Dora-Maira marble: petrologic significance of armoured Si-rich domains, *Eur. J. Mineral.* 17 (2005) 453–464, <https://doi.org/10.1127/0935-1221/2005/0017-0453>.
- [34] S. Timochenko, J.N. Goodier. *Theory of elasticity*, 3rd ed., McGraw Hill, 1970.
- [35] G.E. Beltz, L.B. Freund, On the nucleation of dislocations at a crystal surface, *Phys. Status Solidi B.* 180 (1993) 303–313, <https://doi.org/10.1002/pssb.2221800203>.
- [36] C.E. Carlton, L. Rabenberg, P.J. Ferreira, On the nucleation of partial dislocations in nanoparticles, *Philos. Mag. Lett.* 88 (2008) 715–724, <https://doi.org/10.1080/09500830802307641>.
- [37] J.F. Nye, Some geometrical relations in dislocated crystals, *Acta Metall.* 1 (1953) 153–162, [https://doi.org/10.1016/0001-6160\(53\)90054-6](https://doi.org/10.1016/0001-6160(53)90054-6).
- [38] E. Kröner, On the physical reality of torque stresses in continuum mechanics, *Int. J. Eng. Sci.* 1 (1963) 261–278, [https://doi.org/10.1016/0020-7225\(63\)90037-5](https://doi.org/10.1016/0020-7225(63)90037-5).
- [39] T.J. Ruggles, D.T. Fullwood, Estimations of bulk geometrically necessary dislocation density using high resolution EBSD, *Ultramicroscopy* 133 (2013) 8–15, <https://doi.org/10.1016/j.ultramic.2013.04.011>.
- [40] S. Das, F. Hofmann, E. Tarleton, Consistent determination of geometrically necessary dislocation density from simulations and experiments, *Int. J. Plast.* 109 (2018) 18–42, <https://doi.org/10.1016/j.ijplas.2018.05.001>.
- [41] C.W. Sinclair, W.J. Poole, Y. Bréchet, A model for the grain size dependent work hardening of copper, *Scr. Mater.* 55 (2006) 739–742, <https://doi.org/10.1016/j.scriptamat.2006.05.018>.
- [42] O. Bouaziz, S. Allain, C. Scott, Effect of grain and twin boundaries on the hardening mechanisms of twinning-induced plasticity steels, *Scr. Mater.* 58 (2008) 484–487, <https://doi.org/10.1016/j.scriptamat.2007.10.050>.